Journal of Alloys and Compounds xxx (xxxx) 177610

Contents lists available at ScienceDirect

Journal of Alloys and Compounds

journal homepage: www.elsevier.com/locate/jallcom

Enhanced catalytic combustion of complex VOCs over Ru/Ni-HAP catalyst: Insights into the synergic effects of Ru and Ni species

Yu Wang [a, b], Yijun Jiang [b], Yangyang Yuan [a, *], Li Xu [b, c, **], Wanting Sun [d, e, ***], Si Wu [b], Qingmiao Wang [b], Ning Hu [b], Li Wang [b]

[a] Hangzhou Institute of Advanced Studies, Zhejiang Normal University, Hangzhou 311231, PR China
[b] College of Resources and Environment Engineering, Wuhan University of Science and Technology, Wuhan 430081, PR China
[c] Novel Energy Materials & Catalysis Research Center, Shanwei Innovation Industrial Design & Research Institute, Shanwei 516600, PR China
[d] School of Intelligent Manufacturing, Foshan Polytechnic, Foshan 528137, PR China
[e] School of Engineering, Lancaster University, Lancaster LA1 4YW, United Kingdom

ARTICLE INFO

Keywords:
Hydroxyapatite
Ruthenium
Toluene
Dichloromethane
Catalytic oxidation

ABSTRACT

In this study, Ni was severed as a promoter and impregnated on hydroxyapatite (HAP) to prepare a Ni-doped HAP support, and then Ru was highly dispersed onto the Ni-HAP through urea precipitation method. The synergistic effects between Ru and Ni caused a reduction in the particle size of Ru nanoparticles and an increased Ru^{4+}/Ru^{0} ratios, which was primarily attributed to the strong interaction between the active components and functional groups of OH^{-} and PO_4^{3-}. Meanwhile, Ru/Ni-HAP possessed the highest amount of medium-strength acid sites and relatively low reduction temperatures, indicating the critical balance between acidity and redox capability. Ru/Ni-HAP exhibited superior activity with complete conversion of toluene at 280 °C and DCM at 400 °C, respectively, and such high activity can be maintained throughout the stability tests. Besides, optimal catalytic performance was observed under 600 ppm concentrations of toluene and DCM with a space velocity of 40,000 $ml(g{\cdot}h)^{-1}$. These findings can provide valuable insights for the development of chlorine-resistant catalysts with promising application prospects.

1. Introduction

In recent decades, global air pollution has become increasingly severe with a diversification of pollutants and the volatile organic compounds (VOCs) are regarded as a major source of atmospheric pollution [1]. Generally, VOCs are identified as organic compounds with a saturated vapor pressure higher than 70 Pa at ambient temperature and a boiling point below 260 °C under standard atmospheric pressure [2]. VOCs usually contain a broad spectrum of organic substances such as alkanes, aromatics, alkenes, halogenated hydrocarbons, esters, aldehydes and ketones, which is predominantly derived from industrial processes [3]. In particular, chlorinated volatile organic compounds (CVOCs), such as dichloromethane (DCM), are considered an essential part of VOCs and extensively present in various fields of machinery manufacturing, petrochemicals, pharmaceuticals as well as coating industry [4]. Notably, the release of CVOCs into the environment through evaporation, leakage, and emissions contributes to the depletion of the ozone layer, the formation of photochemical smog, and the exacerbation of global warming. Currently, catalytic combustion has become one of the most effective strategies for treating VOCs, which can provide numerous advantages such as low ignition temperatures, broad adaptability to oxygen concentrations, ease of operation and maintenance, and capable of handling most VOCs [5,6]. Nevertheless, the presence of substantial amounts of CVOCs in VOCs can cause the rapid deactivation of catalysts through site occupation, carbonization and chlorination, and thereby both catalytic efficiency and catalyst lifespan are significantly reduced. Accordingly, addressing the challenge of maintaining catalytic combustion efficiency for CVOC-containing organic waste gases without inducing catalyst poisoning represents one of the most formidable objectives in contemporary research endeavors.

Hydroxyapatite (HAP, $Ca_{10}(PO_4)_6(OH)_2$) has been extensively studied as a porous support material. Due to the ability to exchange cations and anions, HAP can generate new metal-support interactions, and it also exhibits excellent stability and resistance to deactivation [7]. For

* Corresponding author.
** Corresponding author at: College of Resources and Environment Engineering, Wuhan University of Science and Technology, Wuhan 430081, PR China.
*** Corresponding author at: School of Intelligent Manufacturing, Foshan Polytechnic, Foshan 528137, PR China.
E-mail addresses: yuanyangyang@zjnu.edu.cn (Y. Yuan), xuli3021@gmail.com (L. Xu), sunwt_hit@126.com (W. Sun).

https://doi.org/10.1016/j.jallcom.2024.177610
Received 19 September 2024; Received in revised form 4 November 2024; Accepted 13 November 2024
0925-8388/

example, Wang et al. verified the stabilizing effect of the HAP support by comparing the performance Au/CeO_2 catalyst and Au/HAP catalyst, and further elucidated the distinct stabilizing contributions of PO_4^{3-} and OH^- by comparing the performance of Au/HAP catalyst and Au/FAP catalyst with only PO_4^{3-} [8]. Besides, Chlala et al. explored the oxidation of toluene using manganese oxide catalysts supported on HAP, and it can be found that Mn oxide species dispersed on Ca^{2+}-enriched apatite exhibited superior toluene conversion performance [9]. Specifically, Ru has received tremendous attention in recent years due to its capacity to eliminate surface chlorine species via the Deacon reaction, and thereby the catalyst stability can be preserved [10–19]. Liu et al. prepared four catalysts with Ru supported on different carriers (TiO_2, SiO_2, γ-Al_2O_3, ZnO_2), and the Ru/TiO_2 catalyst showed the best catalytic activity because of the strong interaction between Ru and the rutile phase [20]. Additionally, Zhao et al. prepared the Ru/Ti_xSn_{1-x} catalysts by the impregnation approach, and the synergistic effects of Ru-O-Ti and Ru-O-Sn bonds can significantly boost its high catalytic activity [21]. Aouad et al. synergized the Ru/CeO_2-Al_2O_3, Ru/CeO_2 and Ru/Al_2O_3 catalysts for the propylene oxidation. It demonstrated that the Ru/CeO_2-Al_2O_3 catalyst possessed the highest activity due to the uniform dispersion of RuO_2 particles on the Al_2O_3 support, and strong low-temperature reducibility can be realized [22]. In our previous work, a homogeneous urea precipitation method was developed to obtain a high dispersion of the Ru active component onto the HAP support, and the Ru/HAP catalyst with high performance can be achieved [23]. Based on the catalytic characterizations, the samples prepared the by homogeneous urea precipitation method had a mesoporous structure with a larger specific surface area, small Ru nanoparticle sizes, and highly uniform distribution on HAP, which was favorable for the exposure of more active sites. However, the complete oxidation temperature for toluene and DCM with this catalyst remains relatively high, which is not conducive to its broader practical application. Therefore, on the basis of the existing research foundation, it is necessary to further improve the catalytic performance of Ru/HAP catalyst.

Recently, the importance of nickel and the synergic effect of Ni-Ru has been widely reported [24–28]. Wang et al. found that NiO supported on CeO_2 enhanced Lewis acidity and enriched surface oxygen vacancies originating from the interaction of sulfates and metal ions were observed, which led to improved conversion efficiency and CO_x ($CO + CO_2$) selectivity in chlorobenzene oxidation [29]. Additionally, it was also reported that the introduction of metal cations can modulate the redox characteristics and the surface acidity or basicity of catalysts [10]. Reports indicate that the degradation process of CVOCs can be remarkably affected by the presence of Brønsted and Lewis acids on the catalyst surface [30–32]. Meng et al. reported that the order of metal intervention of Ce followed by Ni proved to be favorable for the Ni/HAP catalysts, and the first intervening Ce enhanced the lattice oxygen activity and the dispersion of Ni metal. [33]. Moreover, Gong`s group found the presence of Mg influenced the formation and growth of HAP, resulting in lattice distortion and the formation of a large number of lattice defects in HAP, thus promoting Ni entry into the HAP lattice, thus solving the sintering and deactivation problems in the dry reforming of methane [34]. Considering these factors, it can be deduced that the doping of Ni as a promoter into the Ru/HAP catalyst can potentially foster a robust Ru-Ni-HAP interaction, which may serve to further balance the redox capability and surface acidity of catalyst, thereby enhancing the catalytic performance for the oxidation of VOCs and CVOCs.

In this work, Ni is adopted as a promoter and impregnated onto HAP to obtain a Ni-doped HAP support, and then Ru is highly dispersed onto the Ni-HAP support using the urea precipitation method to synthesize the Ru/Ni-HAP catalyst. Based on the analysis of the physical and chemical properties of both the support and catalyst, as compared to catalysts with the single loading of Ru or Ni, the Ru/Ni-HAP catalyst exhibits an enhanced capability to catalyze redox reactions at lower temperatures, and thereby superior catalytic oxidation performance can be achieved. By manipulating various operating conditions, the operational status of Ru/Ni-HAP catalyst is evaluated under realistic scenarios, which can provide insights and reference value for the development of Ru-doped catalysts.

2. Experimental sections

2.1. Preparation of catalysts

Reagents: Ruthenium (III) chloride ($RuCl_3 \cdot xH_2O$), analytical reagent (AR) grade, Aladdin Reagent Co., Ltd.; Nickel (II) acetate tetrahydrate ($C_4H_6NiO_4 \cdot 4H_2O$), Calcium nitrate ($Ca(NO_2)_2$), Diammonium hydrogen phosphate ($(NH_4)_2HPO_4$), AR, Shanghai Macklin Biochemical Technology Co., Ltd.; Urea (CH_4N_2O), AR, Tianjin Kermel Chemical Reagent Co., Ltd.; Ammonia solution ($NH_3 \cdot H_2O$), Anhydrous ethanol, Toluene, Dichloromethane, AR, Sinopharm Chemical Reagent Co., Ltd.

In this experiment, 15.9 g of $Ca(NO_2)_2$ was dissolved in a mixed solution of 90 ml water and 90 ml of anhydrous ethanol to form solution X. Meanwhile, 8.442 g of $(NH_4)_2HPO_4$ was dissolved in 180 ml water to form solution Y. Solution Y was gradually added into solution X, and the pH value was adjusted to 10.5 using $NH_3 \cdot H_2O$. The mixture was stirred in a water bath at 80 ˚C for 2 h, and then filtered and transferred to a high-pressure reactor. Afterward, the hydrothermal treatment was performed at 120 ˚C in a constant temperature oven for 24 h. After cooling to room temperature, the product was dried and calcined at 500 ˚C in air to obtain HAP support. Subsequently, 3 g of HAP support was grinded into a powder, and then 0.64 g of $C_4H_6NiO_4 \cdot 4H_2O$ (with a theoretical Ni loading of 5 wt%) was dissolved in water. The resulting solution was poured into the HAP powder and thoroughly mixed, followed by impregnation at room temperature for 6 h. After drying and calcining at 500 ˚C in air, the Ni-HAP catalyst can be obtained. Finally, 2 g of the HAP support and Ni-HAP catalyst were grinded into powder and placed into two separate beakers, followed by stirring at 80 ˚C for 12 h. After that, 0.02 g of $RuCl_3 \cdot xH_2O$ (with a theoretical Ru loading of 0.5 wt%) and 1.158 g of urea (with a urea/Ru molar ratio of 200) were added into these two beakers for reaction. The mixture was stirred at 80 ˚C in the dark for 8 h, followed by aging at room temperature for 12 h. The sample was filtered and washed to remove the Cl^- ions. After filtration, drying and calcination at 500 ˚C in air, the Ru/HAP and Ru/Ni-HAP catalysts can be obtained.

2.2. Structural characterizations of catalysts

The phase constitutes of the as-prepared catalysts were elucidated through X-ray diffraction (XRD) analysis performed on a Smart Lab SE X-ray diffractometer. Fourier transform infrared spectroscopy (FT-IR) was conducted on a Cary 600 series FTIR spectrometer with the samples diluted in KBr, and the infrared spectrum ranging from 400 to 4000 cm^{-1} to explore the surface groups and species changes in the catalysts. Transmission electron microscopy (TEM, JEM-F200) was employed to observe the crystalline structure of the catalysts. The elemental distributions of the catalysts were energy-dispersive X-ray spectroscopy (EDS) mapping. X-ray photoelectron spectroscopy (XPS, AXIS SUPRA+) was utilized to probe the surface elemental composition and valence state variations, revealing the chemical environment at the surface of catalysts. Hydrogen temperature-programmed reduction (H_2-TPR) was performed using an AutoChem II 2920 chemisorption analyzer (Micromeritics, USA) to study the redox properties. Furthermore, the surface acidity of the catalysts was assessed using ammonia temperature-programmed desorption (NH_3-TPD) profiles and measured on a VDSorb-9li chemisorption analyzer (Vodo, China).

2.3. Evaluation of catalyst activity

A stainless-steel tube with a length of 450 mm, an outer diameter of 8 mm, and an inner diameter of 6 mm was utilized as the reactor. The temperature of reactor was controlled by an electric heating furnace, and the catalyst dosage was 0.75 g. The total gas flow rate was maintained at 500 ml/min with an air velocity of 40,000 ml $(g{\cdot}h)^{-1}$ and a relative humidity of 50 % (25 ˚C), while the concentration of toluene or DCM was set at 600 ppm. The variations in the concentrations of toluene or DCM before and after the reaction were recorded in real-time using a gas chromatograph (GC-9790II, FULI) equipped with an FID detector, a TCD detector and a nickel conversion furnace. Based on the concentrations before and after the reaction, the conversion of toluene or DCM can act as an indicator of catalyst activity, which can be calculated using the following Eq. (1):

Conversion (%) = (1 - final concentration/initial concentration) × 100%.

3. Results and discussion

3.1. Phase analysis of catalysts

Fig. 1 presents the XRD patterns of the HAP support and the catalysts. The XRD patterns of the four catalysts are consistent with the standard HAP card (PDF#86–0740) with the distinct diffraction peaks at 2θ = 25.9˚, 32.0˚, 32.3˚, 33.2˚, 34.2˚, 46.9˚, and 49.6˚, indicating that the phase constitutes of HAP are maintained unchanged during the preparation and multiple calcination processes [35]. This demonstrates that the as-prepared catalysts possess excellent thermal stability of crystalline structure with strong bonding between the support and active components. Due to the high loading of Ni (5 wt%) in the Ni-HAP and Ru/Ni-HAP catalysts, a weak diffraction peak appears at 2θ = 37.2˚, which corresponds to the NiO (111) crystal plane (PDF#47–1049) [36]. The Ru-related diffraction peaks cannot be detected on the Ru/HAP and Ru/Ni-HAP catalysts, which is likely due to the low loading of Ru (0.5 wt%) and the preparation method. In the urea precipitation method, the nanosized Ru particles (<4 nm) are highly uniformly dispersed on the catalyst surface, which is favorable for the progression of catalytic reaction [37]. Besides, it need to take into accountt that the Ni-Ru alloy might appear in the same diffraction angle of Ru. Combined with the preparation process of the sample, there is a high temperature calcination process at 500 ˚C in air, so it's less likely to form Ni-Ru alloys. In addition, it was found in the previous study [19] that the metallic Ru was converted to the oxidation state after the VOCs catalytic oxidation reaction. Therefore, we reasonably speculated that there is no Ru-Ni alloy in the Ru/Ni-HAP sample.

3.2. Analysis of surface functional groups on the catalysts

Fig. 2 shows the FT-IR spectra of the HAP support and the catalysts, and the surface groups and chemical bonds can be determined. The absorption peaks at 1632 cm^{-1} and 3432 cm^{-1} are attributed to the O-H vibrations of adsorbed water on the catalyst surface [38]. The vibrational absorption peak at 3571 cm^{-1} corresponds to the stretching vibration of hydroxyl groups on the HAP support, while the peak at 1039 cm^{-1} can be assigned to the ν_3 asymmetric stretching vibration of P-O functional groups in the phosphate groups. Besides, the peaks at 566 cm^{-1} and 600 cm^{-1} are associated with the ν_4 bending vibrations of the P-O functional groups in the phosphate groups, while the peak at 961 cm^{-1} is attributed to the ν_1 symmetric stretching vibration of P-O functional groups [39]. The vibrational absorption peak at 474 cm^{-1} is related to the ν_2 bending vibration of P-O functional groups in the phosphate groups [40]. The absorption peaks at 878 cm^{-1} and 1383 cm^{-1} are related to the presence of CO_3^{2-}, suggesting that a small amount of atmospheric carbon dioxide gas participated in the reaction and substituted for PO_4^{3-} during the process [41]. It should be noted that all three catalysts exhibit absorption peaks identical to those of HAP, confirming the loading of Ni and Ru on the HAP support is successfully realized. The bond angles and lengths of the OH^- and PO_4^{3-} groups in the HAP support are larger than those in the Ni-HAP, whereas the Ru/HAP and Ru/Ni-HAP catalysts exhibit the smallest bond angles and lengths. This phenomenon demonstrates that the interactions between the Ru nanoparticles, OH^- and PO_4^{3-} groups in the catalysts are stronger than those of Ni, which can affect the catalytic performance. Due to the addition of active components, the catalytic performance is improved, resulting in more thorough reactions with the gas and more CO_2 involved in the reaction. This leads to more substitution of PO_4^{3-} by CO_3^{2-} and thereby more intense CO_3^{2-} absorption peak.

3.3. Analysis of catalyst surface morphology

Fig. 3 shows the TEM images of Ru/HAP (Fig. 3(a, c, e)) and Ru/Ni-HAP (Fig. 3(b, d, f)) catalysts. As shown in Fig. 3(a) and (b), it reveals that the HAP support prepared via hydrothermal method has a rod-like shape. The size of Ru nanoparticles can be determined by analyzing over 100 particles similar to those shown in Fig. 3(c) and (d), and the distribution of particle size was plotted to calculate the average particle diameter. The Ru particles in the Ru/Ni-HAP catalyst have an average

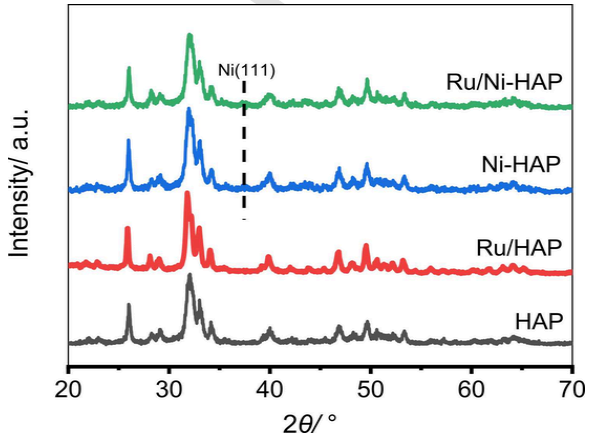

Fig. 1. XRD patterns of the HAP support and the as-prepared catalysts.

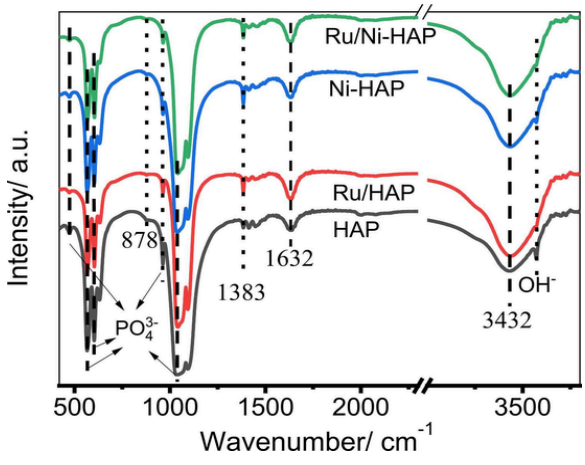

Fig. 2. FT-IR spectra of the HAP support and the as-prepared catalysts.

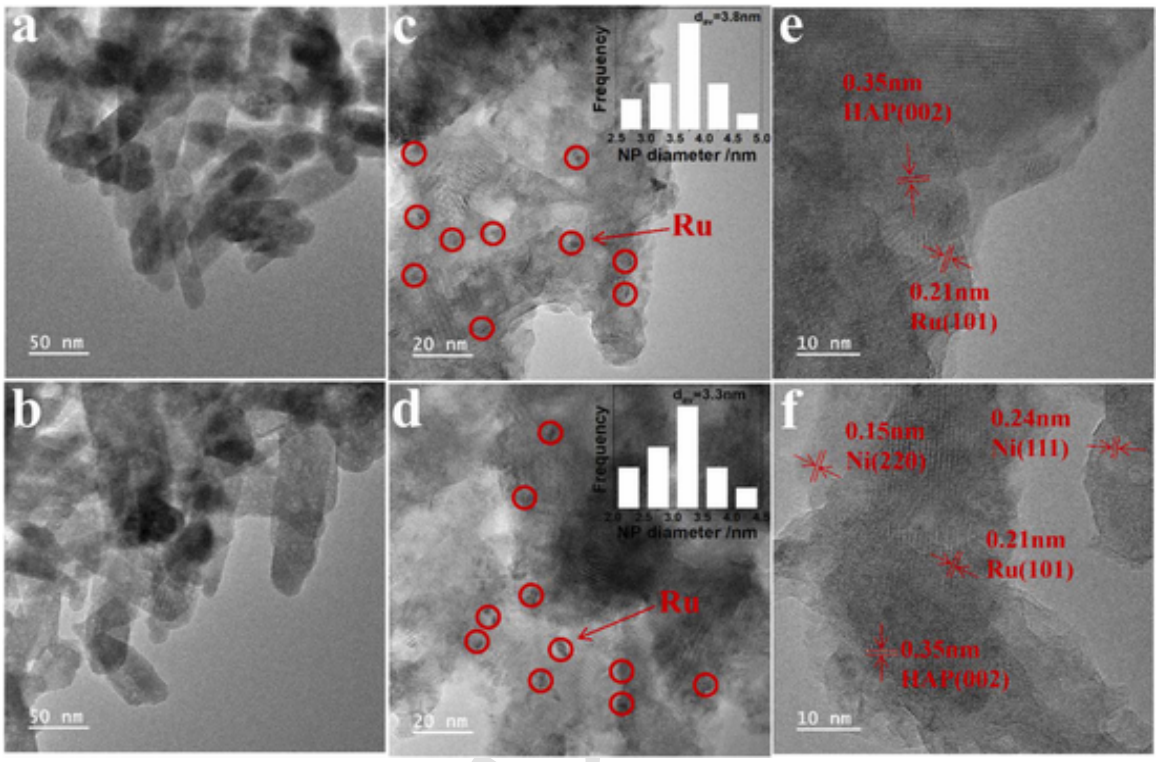

Fig. 3. TEM images (a, c, e) Ru/HAP catalyst and (b, d, f) Ru/Ni-HAP catalyst.

diameter of 3.3 nm, which is smaller than the average diameter of 3.8 nm in the Ru/HAP catalyst. This size reduction is attributed to the fact that the doping of Ni can cause the interaction between Ru and Ni, and the dispersion of Ru particles on HAP is promoted, resulting in smaller Ru particles with a larger surface area in contact with the reaction gases to facilitate the progress of reaction [42]. Further analysis using high-resolution TEM as presented in Fig. 3(e) and (f), it reveals that the lattice fringes with the widths of 0.35 nm and 0.21 nm are assigned to the (002) plane of HAP (PDF#86–0740) and the (101) plane of Ru (PDF#88–1734), respectively. Moreover, as shown in Fig. 3(f), the lattice fringes with widths of 0.15 nm and 0.24 nm are assigned to the (220) and (111) planes of NiO (PDF#47–1049), which is consistent with the above XRD analysis [43]. In order to verify the spatial distribution of different elements in the Ru/HAP and Ru/Ni-HAP catalysts, EDS mapping analysis was performed on the catalysts, as shown in Fig. 4. It is apparent that the Ca, P, O, Ru, and Ni elements are uniformly distributed on the catalyst surface. Meanwhile, the widely dispersed Ca, O and P elements are consistent with the structure of HAP itself. Specifically, for the Ru/Ni-HAP catalyst, the Ru and Ni elements also exhibit good dispersibility on the catalyst surface. Fig. 4(b) shows that the Ni element distribution is greater than that of Ru, which is due to the higher loading amount of Ni (5 wt%) compared to Ru (0.5 wt%). This can validate the experimental design that both Ru/HAP and Ru/Ni-HAP catalysts are successfully achieved.

3.4. Analysis of element valence states on the catalyst surface

Fig. 5 shows the XPS analysis of the HAP support and the catalysts. As presented in Fig. 5(a), the peaks at 854.4 eV and 872.0 eV correspond to the Ni $2p_{3/2}$ and Ni $2p_{1/2}$ orbitals of Ni^{2+}, which are associated with the characteristics of NiO [44]. It indicates that Ni in the catalyst predominantly exists as Ni^{2+}, which is consistent with the diffraction peaks of NiO detected by XRD. The peaks at 856.1 eV and 873.7 eV can be assigned to the Ni $2p_{3/2}$ and Ni $2p_{1/2}$ orbitals of Ni^{3+} corresponding to Ni_2O_3. The presence of Ni^{3+} is likely due to the susceptibility of Ni^{2+} to oxidation by atmospheric oxygen on the catalyst surface during the preparation and calcination processes [45], while the S_1 and S_2 represent the relevant satellite peaks. As shown in Fig. 5(b), both the Ru/HAP and Ru/Ni-HAP catalyst surfaces exhibit the presence of Ru^0 metal and RuO, while the peaks at 460.6 eV and 483.0 eV correspond to the Ru 3p orbitals of Ru^0 metal [46]. The formation of Ru^0 metal may be attributed to the presence of Cl^- ions, which can be adhered to the surface of Ru species and avoid oxidation during the calcination process. The peaks at 462.3 eV and 484.7 eV correspond to the Ru 3p orbitals of Ru^{4+} [47]. Despite the protective effect of Cl^- ions against the oxidation of Ru, sufficient oxygen exposure can cause the oxidation of more Ru to Ru^{4+}. Fig. 5(c) and (d) show that the addition of Ni and Ru has minimal impact on the peak positions of Ca and P, indicating that the calcium-phosphate structure of HAP remains unaffected during the preparation and calcination processes, which is consistent with the XRD results. Besides, a quantitative analysis of the Ni^{3+}/Ni^{2+} and Ru^{4+}/Ru^0 ratios in the catalysts was performed based on the peak area ratios. It can be found that with the addition of Ru, the electron lost by Ni^{2+} is decreased, and the Ni^{3+}/Ni^{2+} ratio is reduced from 2.12 (Ru/HAP) to 2.03 (Ru/Ni-HAP) without affecting the peak positions of the Ni 2p orbitals. Due to the doping of Ni, the position of Ru^{4+} characteristic peak in the Ru/Ni-HAP catalyst is shifted left by 0.3 eV, suggesting that the interaction between Ru and Ni can affect the variation of Ru. The Ru^{4+}/Ru^0 ratio is increased from 2.10 (Ru/HAP) to 2.21 (Ru/Ni-HAP), and the increase in Ru^{4+} is beneficial for improving the interaction between the active component Ru and the support, thereby facilitating the catalytic reaction.

3.5. Analysis of catalyst redox properties

To investigate the reduction properties of the catalyst surface species, H_2-TPR measurements were conducted and shown in Fig. 6. By

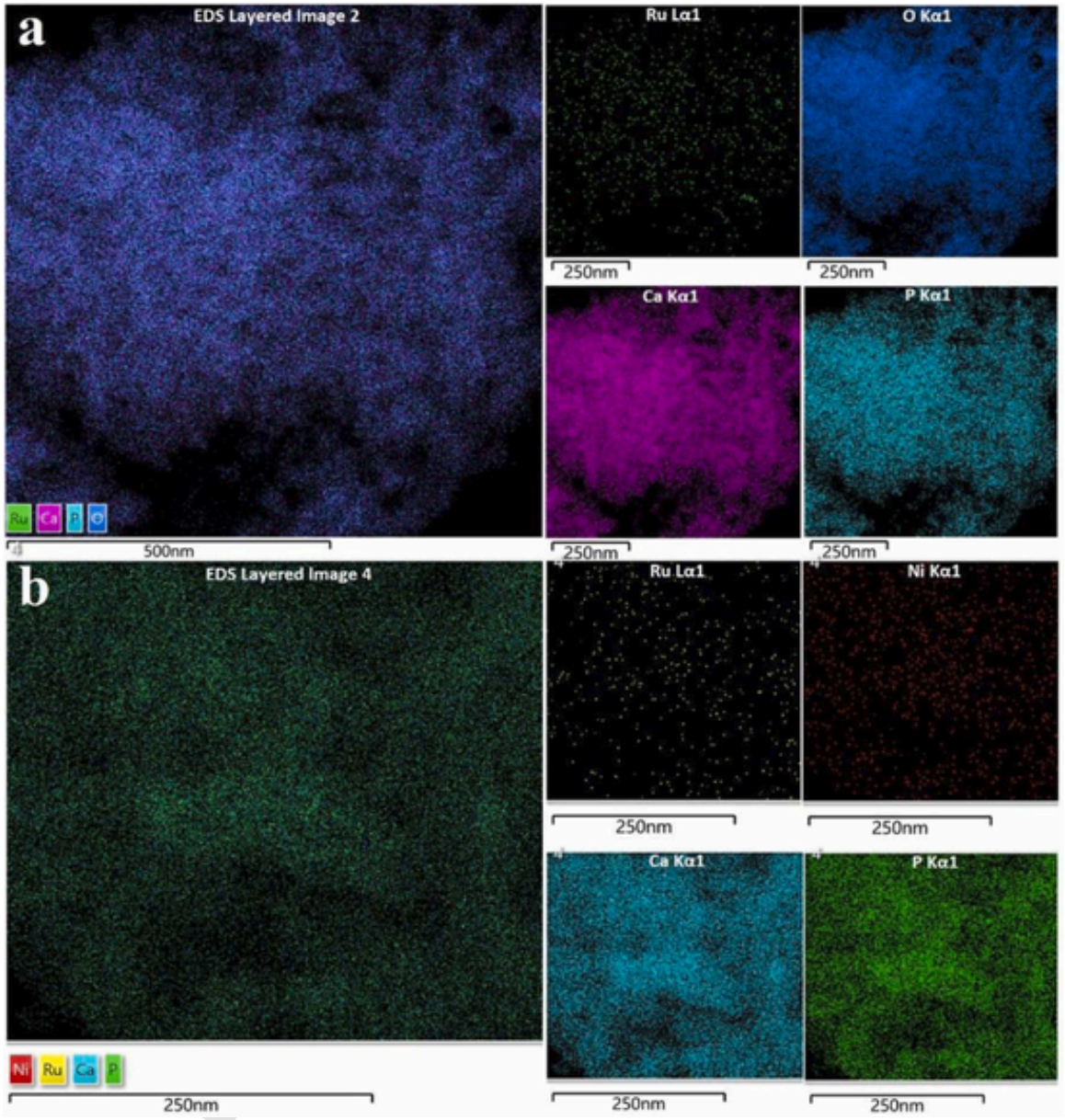

Fig. 4. EDS mappings of (a) Ru/HAP catalyst and (b) Ru/Ni-HAP catalyst.

curve fitting, the H_2 consumption values corresponding to the reduction peaks were calculated and are depicted in. For all samples, a broad high-temperature peak appears between 605 ˚C and 703 ˚C, which is attributed to the dehydroxylation process of HAP support [48]. The reduction temperature of HAP in both Ni-HAP and Ru/Ni-HAP catalysts is dramatically decreased by approximately 80 ˚C, indicating that the doping of Ni can improve the reduction of HAP. Ni can promote more lattice oxygen to participate in the reduction of HAP (H_2 consumption increased from 3.52 mmol/g to 11.73 and 13.80 mmol/g, whereas the addition of Ru exerts a negligible influence on this process (The reduction temperature (703 ˚C) and H_2 consumption of HAP (3.20 mmol/g) almost unchanged over Ru/HAP). The reduction peak detected at 346 ˚C in Ni-HAP catalyst corresponds to the conversion of NiO into Ni. This reduction is also enhanced by the addition of Ru, since the peak temperature shifted from 346 ˚C to 290 ˚C over Ru/Ni-HAP catalyst, once again, confirming the strong interaction between Ru and Ni. For the RuO_x species over Ru/HAP, the peaks observed at 118 ˚C to 168 ˚C are associated with the reduction of highly active and smaller-sized Ru particles, which exhibit rapid reduction kinetics [49]. Conversely, the hydrogen consumption peaks observed at 395 ˚C are attributed to the reduction of less active and larger-sized Ru particles, which undergo reduction at a slower rate. Obviously, the reduction of RuO_x species at 111 and 356 ˚C is greatly improved due to the doping of Ni over Ru/Ni-HAP. By comprehensive comparison, for the optimal Ru/Ni-HAP catalyst, the reduction of RuO_x species (118–168 ˚C moved to 111 ˚C, 395 ˚C moved to 356 ˚C), NiO species (346 ˚C moved to 290 ˚C), and lattice oxygen in HAP (700 ˚C moved to 605 ˚C), are significantly increased due to the strong synergistic promoting effect between Ru, Ni and HAP. Owing to the synergistic effect of Ni and Ru, the reduction temperatures of both large and small Ru particles in the Ru/Ni-HAP catalyst are shifted to lower temperatures as compared to the Ru/HAP catalyst, and the consumption of reduction peaks are significantly increased [50]. This indicates an enhanced redox capability of catalyst, which is conducive to the oxidation of oxygen with toluene and DCM at lower temperatures. The decrease in the number of large Ru particles and the increase in smaller Ru particles can result in a diminished average parti-

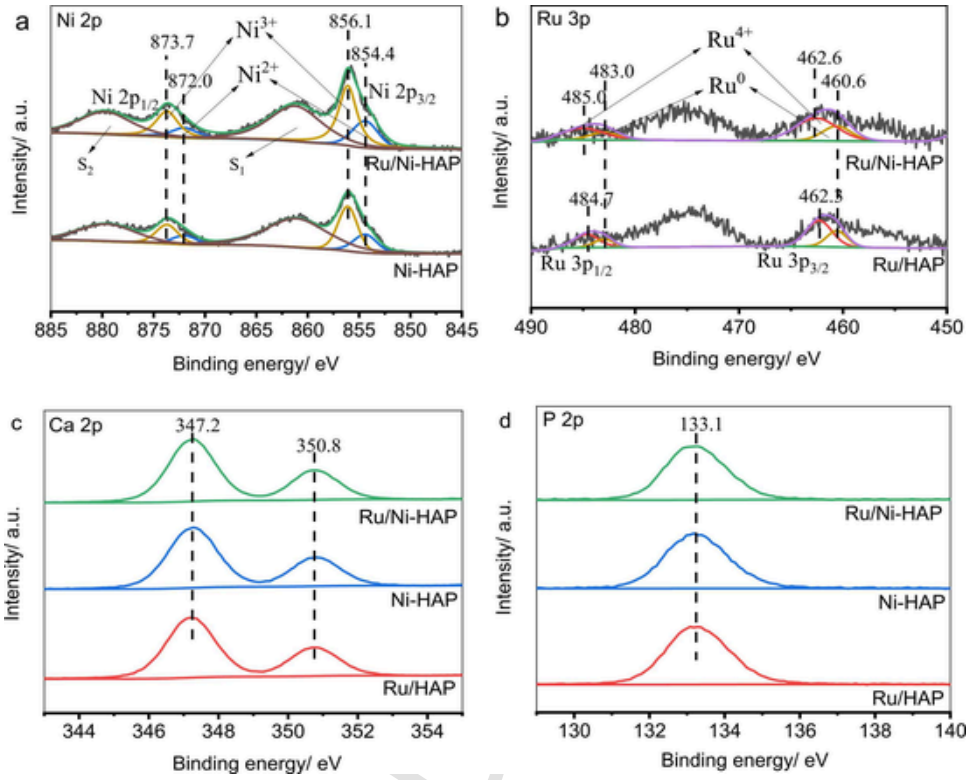

Fig. 5. XPS spectra of Ru/HAP catalyst, Ni-HAP catalyst and Ru/Ni-HAP catalyst: (a) Ni 2p, (b) Ru 3p, (c) Ca 2p and (d) P 2p.

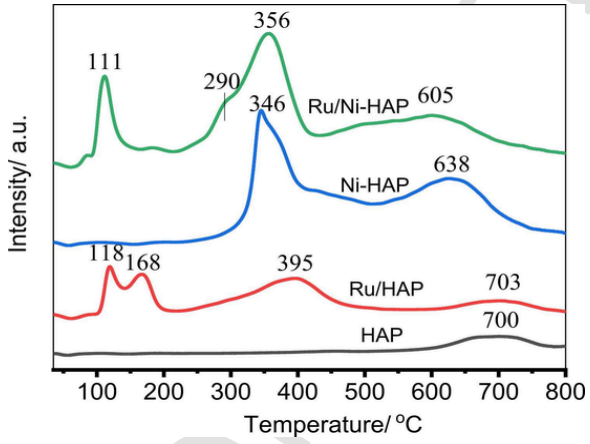

Fig. 6. H_2-TPR curves of the HAP support and the as-prepared catalysts.

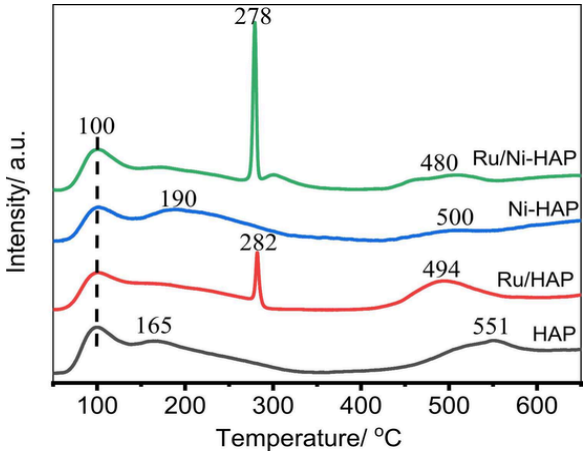

Fig. 7. NH_3-TPD curves of the HAP support and the as-prepared catalysts.

cle diameter and an increased contact area with the reacting gases [51], which is consistent with the particle sizes observed in the TEM images.

3.6. Analysis of surface acidity on catalysts

HAP has the rare property of containing both acid and basic sites in its inherent structure, which is strongly correlated to the Ca/P atomic ratio in the calcium phosphate compound. Herein, HAP has a Ca/P of ca.1.67 with Ni and Ru doping, which should possess both acidic and basic sites, and the acid sites was detected by NH_3-TPD, as shown in Fig. 7. Because the acid sites were reported to be the core active sites for dechlorination reaction (Lewis acid and Brønsted acid) and C-C band cleavage (Lewis acid), and the enhancement of Lewis acid can suppress the accumulations of Cl and coke on catalyst surface, thus promoting stability in toluene and DCM oxidation [16]. The relative acid amounts were also calculated using the desorption peak areas by curve fitting. All four samples exhibit certain acidic properties. Based on the different desorption temperatures of NH_3, the acidity can be categorized into weak acidic sites below 200 °C, medium-strong acidic sites between 200 °C and 400 °C, and strong acidic sites above 400 °C [31]. The HAP support shows NH_3 adsorption peaks at 100 °C, 165 °C and 551 °C, indicating the presence of multiple weak and strong acidic sites [52]. For the Ni-HAP catalyst, the adsorption peaks at 100 °C and 190 °C correspond to the adsorption of NH_3 on weak acid sites, while the peak at 500 °C is attributed to the adsorption of NH_3 on strong acid sites [30]. As compared to the HAP support, some weak acidic sites are shifted to higher

temperatures, and the NH_3 desorption increased from 5.11 to 6.08 mmol/g, indicating that the number of weak acidic sites is increased. Conversely, the strong acidic sites are shifted to lower temperatures, and the NH_3 desorption decreased from 4.69 to 1.30 mmol/g. As compared to the HAP and Ni-HAP catalyst, the Ru-contained catalysts show a reduction in weak acidic sites but an appearance of new NH_3 desorption peak at around 280 °C, which is ascribed to the adsorption of NH_3 on medium-strong acid sites. In particular, compare to Ru/HAP, Ru/Ni-HAP exhibits much more medium-strong acidic sites, the NH_3 desorption increased nearly three times (from 0.29 to 0.86 mmol/g). This phenomenon suggesting that the addition of Ni enhanced the synergistic effect between Ru and Ni, thus produce more medium-strong acid sites. And the increased acidity can improve the catalytic oxidation performance of the Ru/Ni-HAP catalyst when facing C-Cl bonds [53]. In terms of the strong acid sites, the addition of Ru causes the strong acidic sites on the catalyst to be shifted to lower temperatures. The HAP support and Ru/HAP catalyst exhibit broad strong acid peaks, while the Ni-HAP and Ru/Ni-HAP catalysts show smooth curves for strong acid peaks. The order of NH_3 desorption follows the sequence of HAP > Ru/HAP > Ru/Ni-HAP > Ni-HAP, indicating that the strong acid sites of HAP decreased by the Ni and Ru doping. As expect, excessively strong acid sites could lead to the decreased redox performance of the catalyst. Therefore, the synergistic doping of Ru and Ni effectively regulates the surface acidity of HAP, thus achieving a balance between redox capacity and acidity of Ru/Ni-HAP catalyst [54].

3.7. Analysis of catalyst activity and stability

Fig. 8 illustrates the reaction activity curves for the oxidation of toluene and DCM by the catalysts. The T_{50} and T_{90} values of the catalysts are listed in. As shown in Fig. 8(a), the catalytic efficiency of toluene oxidation over the different catalysts is decreased in the following order Ru/Ni-HAP > Ru/HAP > Ni-HAP > HAP. The HAP support exhibits a low catalytic efficiency of less than 25 % throughout the reaction. In contrast, the Ru/Ni-HAP catalyst shows the highest toluene conversion with a T_{50} temperature of 266 °C, which is lower than that of Ni-HAP (300 °C) and Ru/HAP (281 °C). The T_{90} temperature for Ru/Ni-HAP catalyst is determined as 277°C, which is lower than those for the Ni-HAP (288 °C) and Ru/HAP (329 °C) catalysts, and the Ru/Ni-HAP catalyst reaches the complete conversion of toluene at 280 °C.

Fig. 8(b) presents the DCM conversion of the HAP support and the catalysts. It can be observed that the HAP support has a DCM oxidation efficiency of less than 20 %. The Ru/Ni-HAP catalyst exhibits superior oxidation efficiency with a T_{50} temperature of 343 °C, which is lower than the Ni-HAP (421 °C) and Ru/HAP (368 °C). The T_{90} temperature for Ru/Ni-HAP catalyst is determined as 380°C, which is lower than those for the Ni-HAP (476 °C) and Ru/HAP (414 °C) catalysts, and the Ru/Ni-HAP catalyst reaches the complete conversion of DCM at 400 °C. From the aforementioned results, it is apparent that as the temperature is increased, there is a certain conversion for the combustion of toluene and DCM in air, thus the activity of the HAP support can be considered negligible. Since catalytic oxidation of DCM is possible to generate by-products including CH_3Cl, $CHCl_3$ and CCl_4, the products of DCM oxidation over Ru/Ni-HAP catalyst was conducted as shown in. During the oxidation process, the catalyst exhibited a relatively low selectivity for CO. The maximum CO yield of 3.6 % was achieved at 340 °C, and the main product is determined as CO_2. implied the by-products $CHCl_3$ and CCl_4 were generated, rather than CH_3Cl. As the temperature increases, the yield of by-products is firstly increased and then decreased, and the amount of by-products was limited (less than 0.5 %). Based on above analysis, Ru/Ni-HAP catalyst boasted excellent balance of acidity and redox capacity, thereby more active oxygen species can involve the reaction, resulting in the elevation of catalytic activity and selectivity.

Fig. 8(c) and (d) show the Arrhenius plots of reaction rates for the HAP support and the catalysts. The activation energy (E_a) for the oxidation reactions is determined by the slope of the fitted lines, presented the recently reported works of catalysts for toluene and DCM oxidation, respectively. As listed in, the E_a for the oxidation of toluene on the Ru/Ni-HAP catalyst is 174 kJ/mol, which is significantly lower than that for the Ru/HAP (266 kJ/mol) and Ni-HAP (345 kJ/mol) catalysts. In the case of DCM oxidation on the Ru/Ni-HAP catalyst, the E_a is 108 kJ/mol, exceeding those for the Ru/HAP (141 kJ/mol) and Ni-HAP (174 kJ/mol) catalysts. The low activity of Ni-HAP can be attributed to the absence of medium-strong acid sites, while the single non-noble metal Ni has weak oxidation capability for toluene and DCM so more energy for catalytic oxidation is required [55]. The single noble metal Ru is also less effective than the bimetallic Ru/Ni, where Ru plays a crucial role in the reaction. For the oxidation of DCM, the Deacon reaction is more likely to occur. The addition of Ni leads to smaller Ru particles, and thereby the catalyst surface area in contact with the gas is increased, accelerating the reaction rate, and diminishing the required activation energy. Eventually, the Ru/Ni-HAP catalyst exhibits the best catalytic performance.

To evaluate the long-term efficiency of the Ru/Ni-HAP catalyst, the stability under high temperatures and in the presence of chlorine was tested, and the corresponding results are shown in Fig. 8(e) and (f). The stability tests were conducted for 100 h, and the toluene and DCM reactions were performed at temperatures of 280 °C and 400 °C, respectively. It can be found that throughout the test, the toluene and DCM conversion are maintained consistently around 99 %, suggesting that the Ru/Ni-HAP catalyst exhibits excellent stability and high thermal resistance. Particularly for DCM, the activity of Ru/Ni-HAP catalyst can be maintained without deactivating due to chlorine accumulation, demonstrating its remarkable chlorine resistance.

Based on characterizations and catalytic activities, we proposed that the synergism of acid and redox properties is the key factor to design active catalysts for the catalytic oxidation of toluene and DCM. A large enhancement of the DCM oxidation rate was observed with the catalyst with the highest medium-strong acidic sites, i.e. the Ru/Ni-HAP. The reaction rates were further altered by the redox behaviors of the catalysts. The better acid and redox properties of the catalyst offer greater advancements in oxidation of toluene and DCM, in agreement with the findings of Weng [56,57] and Dai [58]. According to the analysis of XPS, H_2-TPR and NH_3-TPD, the strong interaction between Ru and Ni endows the Ru/Ni-HAP catalyst with the best redox capability, and thereby the oxidation of toluene and DCM can be realized at lower temperatures. The introduction of Ru and Ni into the catalyst can produce the largest amount of medium-strong acid sites, which can promote the broken of C-H bonds in toluene and C-Cl bonds in DCM to facilitate the progress of the catalytic reaction.

3.8. Analysis of catalyst performance under various operating conditions

To investigate the catalytic performance of Ru/Ni-HAP catalyst under different operating conditions, the experiments were conducted by varying the concentrations of toluene and DCM (300, 600, 1200 ppm, with GHSV = 40,000 $ml(g{\cdot}h)^{-1}$) and the air velocity (600 ppm, with GHSV = 20,000, 40,000, 80,000 $ml(g{\cdot}h)^{-1}$) to simulate actual scenarios that might be encountered, and Fig. 9 shows the corresponding catalytic activity. There is a noticeable decrease in the catalytic activity of the Ru/Ni-HAP catalyst with the increased reactant concentration and air velocity, leading to a significant rise in the reaction temperature required for complete conversion. However, when the reaction proceeds for a period, and the concentration of toluene or DCM, or the air velocity is reduced, the activity of catalyst reverts to its previous level. This demonstrates that the catalyst cannot become deactivated under prolonged exposure to high concentrations of toluene and DCM. The catalytic performance can be optimized by adjusting the reaction time and

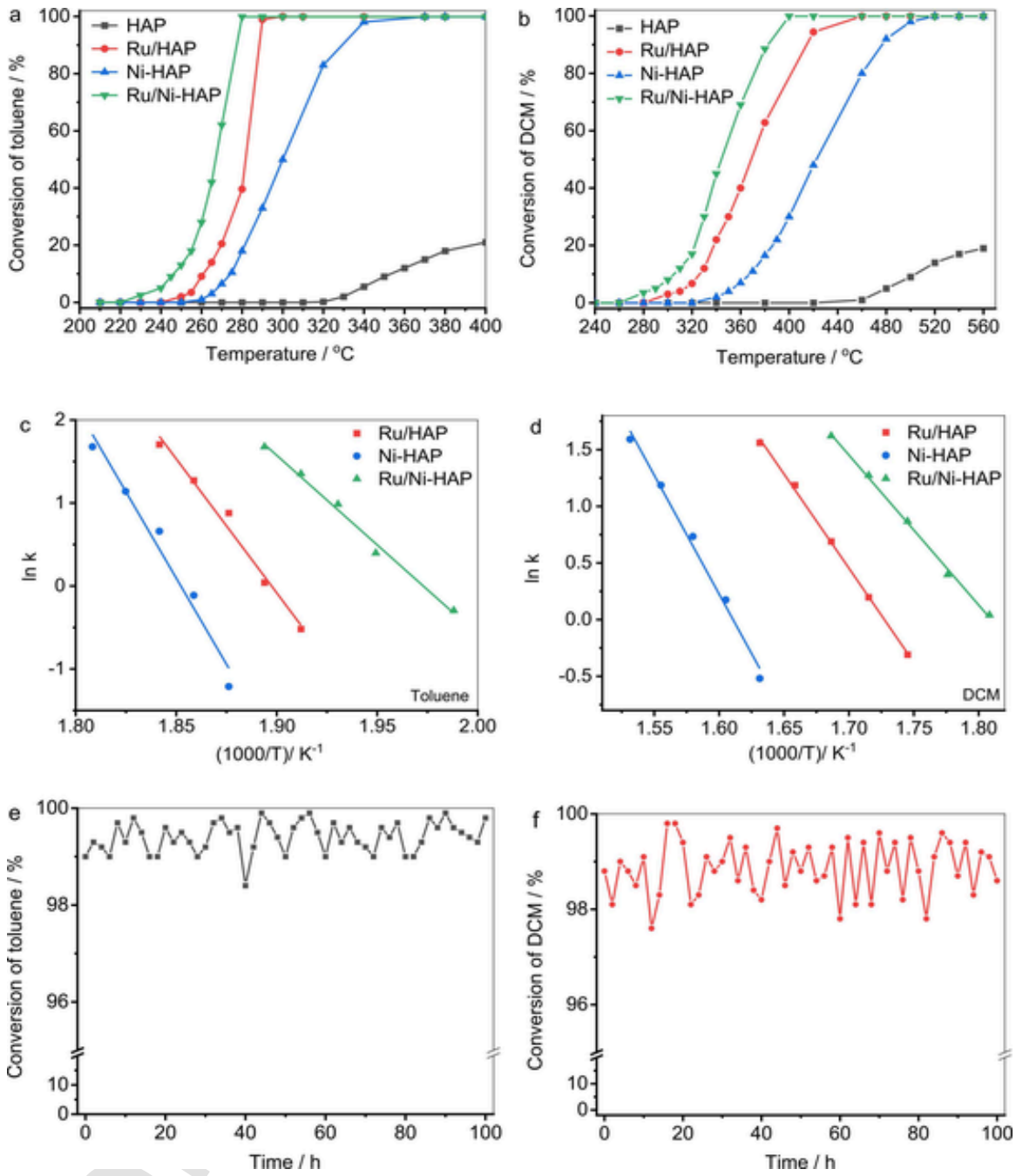

Fig. 8. The reaction activity curves for the oxidation of toluene and DCM by the HAP support and the catalysts: (a, b) Conversions; (c, d) Arrhenius curves; (e, f) Stability test of Ru/Ni-HAP catalyst.

temperature under varying conditions, which is beneficial for enhancing the conversion and achieving complete degradation of toluene or DCM. Alternatively, diluting the concentration of VOCs or reducing the airflow can also promote the progress of the catalytic reaction, and this approach can provide effective regulation of the catalytic reaction system based on actual site conditions.

Based on the above discussion, we proposed the catalytic mechanism of VOCs on Ru/Ni-HAP catalyst. First, toluene and DCM molecules interacted with HAP support through physical adsorption or chemical adsorption, in particular, the hydroxyl group on HAP played an pivotal role in promoting the dechlorination of DCM, which has been reported in the literature [57,59], such a reaction is formed both on dehydroxylated and fully hydroxylated surfaces via dual-site interaction (OH···π–electron and OH···Cl) [53]. Toluene and DCM molecules can also undergo a dehydrogenation with the acidic sites of catalyst to produce an adsorbed state of intermediates [60], which were activated by heating to promote the corresponding reaction. During the catalytic oxidation of toluene and DCM, Ru^{4+} and Ni^{2+} with excellent redox properties played dominant roles, which can change the electronic state, activate the adsorbed reactant molecules, make them more prone to degrade. With reaction temperature rised, the active oxygen and lattice oxygen species on Ru^{4+} and Ni^{2+} can totally oxidize toluene and DCM into CO_2, H_2O and HCl/Cl_2, then, the Ni^0 and Ru^0 was re-oxidized to NiO and RuO_2 by capturing oxygen in the feed gas. Finally, these prod-

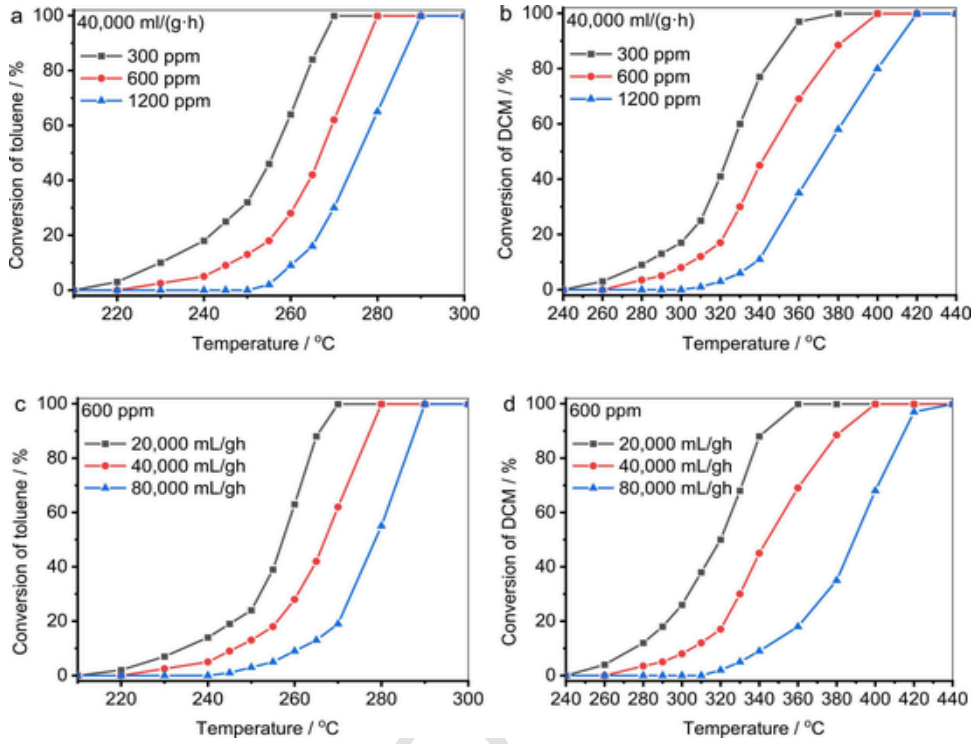

Fig. 9. (a, b) Catalytic activity curves of Ru/Ni-HAP catalyst for catalytic combustion of toluene and DCM at different concentrations; (c, d) Catalytic activity curves of Ru/Ni-HAP catalyst for catalytic combustion of toluene and DCM at different space velocities.

ucts can be dissociated from the surface of catalyst and released to the tail gas.

4. Conclusion

In this study, the HAP support is prepared using the hydrothermal method, and Ni is loaded onto HAP by the impregnation method to fabricate the Ni-HAP catalyst. Ru is then successfully loaded onto both HAP and Ni-HAP using the urea precipitation method to prepare the Ru/HAP and Ru/Ni-HAP catalysts. The structures of as-prepared catalysts are comprehensively characterized, and the resultant catalytic activities are evaluated. The main conclusion can be drawn as follows.

(1) As compared to the single Ni metal, the addition of noble metal Ru can enhance the interactions with OH^- and PO_4^{3-} groups in HAP, and both the amount of medium-strong acidic sites and the overall acidity are increased, leading to the improved catalytic activity.
(2) The co-doping of Ru and Ni can bring about a proliferation of smaller Ru particles and a concomitant reduction in larger Ru particles, leading to a diminished average particle diameter, an expanded specific surface area, and an increased Ru^{4+}/Ru^0 ratio. This enrichment of active Ru^{4+} species is conducive to the exposure of a larger number of active sites for engagement in the catalytic reaction.
(3) With the combination of H_2-TPR and NH_3-TPD analyses, it demonstrates that the synergistic interaction between Ru and Ni can modulate the acidity and redox characteristics of catalyst. The Ru/Ni-HAP catalyst exhibits a significant increase in medium-strong acidic sites, a decrease in strong acidic sites and a reduced reduction temperature, indicating that the redox property is enhanced. By comparisons, the Ru/Ni-HAP catalyst possesses the most rapid reaction kinetics and requires the least activation energy for the complete conversion of toluene and DCM, suggesting that exceptional catalytic efficacy can be achieved. The stability assessments confirm that no signs of deactivation can be detected in the Ru/Ni-HAP, and its adaptability across various operating conditions underscores the significant potential for practical applications.

CRediT authorship contribution statement

Li Wang: Investigation. **Yangyang Yuan:** Data curation. **Ning Hu:** Investigation. **Li Xu:** Supervision, Resources, Formal analysis. **Si Wu:** Investigation, Formal analysis. **Yu Wang:** Investigation, Formal analysis. **Yijun Jiang:** Investigation, Formal analysis. **Wanting Sun:** Writing – review & editing, Writing – original draft.

Declaration of Competing Interest

The authors declare that they have no competing interests. This research was conducted without any commercial or financial relationships that could be construed as a potential conflict of interest. All the authors have contributed significantly to the research and have read and approved the final version of the manuscript. No financial support was received for this study, and there are no relevant financial or other interests to disclose.

Acknowledgment

This work was supported by the National Natural Science Foundation of China (No. 21906125), the Special Foundation for Key Fields of Colleges and Universities in Guangdong Province (2021ZDZX4094), and “The 14th Five Year Plan” Hubei Provincial advantaged characteristic disciplines (groups) project of Wuhan University of Science and Technology (No. 2023A0302). The authors would like to thank the Analysis and Testing Center of Wuhan University of Science and Technology for analytical support.

Data availability

No data was used for the research described in the article.

References

[1] M.S. Hussain, G. Gupta, R. Mishra, N. Patel, S. Gupta, S.I. Alzarea, I. Kazmi, P. Kumbhar, J. Disouza, H. Dureja, N. Kukreti, S.K. Singh, K. Dua, Unlocking the secrets: Volatile Organic Compounds (VOCs) and their devastating effects on lung cancer, Pathol. - Res. Pract. 255 (2024) 155157.

[2] C. Yang, G. Miao, Y. Pi, Q. Xia, J. Wu, Z. Li, J. Xiao, Abatement of various types of VOCs by adsorption/catalytic oxidation: a review, Chem. Eng. J. 370 (2019) 1128–1153.

[3] Y. Wu, J. Qian, J. Xing, J. Li, H. Huang, Y. Wang, J. Xu, Impact of Cu content on the activity of TiO2-based catalysts for toluene oxidation, J. Alloy. Compd. 1005 (2024) 176095.

[4] Q. Ying, Y. Liu, H. Li, Y. Zhang, Z. Wu, A comparative study of the dichloromethane catalytic combustion over ruthenium-based catalysts: unveiling the roles of acid types in dissociative adsorption and by-products formation, J. Colloid Interface Sci. 605 (2022) 537–546.

[5] Y. Hao, S. Chen, L. Wu, R. Chen, P. Sun, T. Chen, Hierarchically porous silica supported ceria and platinum nanoparticles for catalytic combustion of toluene, J. Alloy. Compd. 867 (2021) 159030.

[6] L. Li, Y. Jin, M. Wei, R. Wang, Z. Fei, Pt-modified 3D MnCoOx nanocages as effective catalysts for toluene oxidation, J. Alloy. Compd. 955 (2023) 170257.

[7] M. Kalaiyarasan, S.M. Bharathi, N. Rajendran, P. Bargavi, R. Ramya, K. Saranya, B.S. Kumar, R. Pratibha, Synergetic effect of Fe/Ag ions incorporated HAp on AZ31 Mg alloy to improve corrosion resistance and osteogenic activity, J. Alloy. Compd. 960 (2023) 170711.

[8] Y. Wang, B.-b Chen, M. Crocker, Y.-j Zhang, X.-b Zhu, C. Shi, Understanding on the origins of hydroxyapatite stabilized gold nanoparticles as high-efficiency catalysts for formaldehyde and benzene oxidation, Catal. Commun. 59 (2015) 195–200.

[9] D. Chlala, J.M. Giraudon, N. Nuns, C. Lancelot, R.-N. Vannier, M. Labaki, J.F. Lamonier, Active Mn species well dispersed on Ca2+ enriched apatite for total oxidation of toluene, Appl. Catal. B: Environ. 184 (2016) 87–95.

[10] F. Lin, Z. Zhang, N. Li, B. Yan, C. He, Z. Hao, G. Chen, How to achieve complete elimination of Cl-VOCs: a critical review on byproducts formation and inhibition strategies during catalytic oxidation, Chem. Eng. J. 404 (2021) 126534.

[11] Y. Wang, P. Wang, X. Lu, N. Hu, Q. Wang, S. Wu, W. Deng, L. Wang, Construction of mesoporous Ru@ZSM-5 catalyst for dichloromethane degradation: synergy between acidic sites and redox centres, Fuel 346 (2023) 128337.

[12] K. Shen, B. Gao, H. Xia, W. Deng, J. Yan, X. Guo, Y. Guo, X. Wang, W. Zhan, Q. Dai, Oxy-anionic doping: a new strategy for improving selectivity of Ru/CeO2 with synergetic versatility and thermal stability for catalytic oxidation of chlorinated volatile organic compounds, Environ. Sci. Technol. 56 (2022) 8854–8863.

[13] X. Lv, M. Jiang, J. Chen, D. Yan, H. Jia, Unveiling the lead resistance mechanism and interface regulation strategy of Ru-based catalyst during chlorinated VOCs oxidation, Appl. Catal. B: Environ. 315 (2022) 121592.

[14] Y. Wang, Z. Liu, Y. Wei, Y. Hu, Y. Chen, B. Shan, B. Wu, Significant inhibition of secondary pollution in the catalytic oxidation of chloroaromatics over a bifunctional Ru1/CeO2 single-atom catalyst, J. Mater. Chem. A 12 (2024) 2949–2958.

[15] Y. Wang, C. Du, Z. Liu, Y. Liu, B. Shan, L. Guo, R. Chen, Highly active and durable chlorobenzene oxidation catalyst via porous atomic layer coating of Ru on Pt/Al2O3, Appl. Catal. B: Environ. 330 (2023) 122648.

[16] Y. Wang, G. Wang, W. Deng, J. Han, L. Qin, B. Zhao, L. Guo, F. Xing, Study on the structure-activity relationship of Fe-Mn oxide catalysts for chlorobenzene catalytic combustion, Chem. Eng. J. 395 (2020) 125172.

[17] Y. Wang, Y. Chen, L. Zhang, G. Wang, W. Deng, L. Guo, Total catalytic oxidation of chlorinated aromatics over bimetallic Pt–Ru supported on hierarchical HZSM-5 zeolite, Microporous Mesoporous Mater. 308 (2020) 110538.

[18] G. Wang, Y. Wang, L. Qin, B. Zhao, L. Guo, J. Han, Efficient and stable degradation of chlorobenzene over a porous iron–manganese oxide supported ruthenium catalyst, Catal. Sci. Technol. 10 (2020) 7203–7216.

[19] Y. Wang, D. Yang, S. Li, M. Chen, L. Guo, J. Zhou, Ru/hierarchical HZSM-5 zeolite as efficient bi-functional adsorbent/catalyst for bulky aromatic VOCs elimination, Microporous Mesoporous Mater. 258 (2018) 17–25.

[20] X. Liu, J. Zeng, J. Wang, W. Shi, T. Zhu, Catalytic oxidation of methyl bromide using ruthenium-based catalysts, Catal. Sci. Technol. 6 (2016) 4337–4344.

[21] J. Zhao, W. Xi, C. Tu, Q. Dai, X. Wang, Catalytic oxidation of chlorinated VOCs over Ru/TixSn1-x catalysts, Appl. Catal. B: Environ. 263 (2020) 118237.

[22] S. Aouad, E. Abi-Aad, A. Aboukaïs, Simultaneous oxidation of carbon black and volatile organic compounds over Ru/CeO2 catalysts, Appl. Catal. B: Environ. 88 (2009) 249–256.

[23] L. Xu, J. Wan, P. Wang, W. Sun, Y. Wang, A novel Ru loaded hydroxyapatite catalyst prepared by a facile and efficient deposition method for catalytic oxidation of toluene and dichloromethane, Catal. Lett. (2024), https://doi.org/10.1007/s10562-024-04782-z.

[24] A. S, T. B, V. G, D. S, N. Kulal, A. S, Framework of ruthenium-containing nickel hydrotalcite-type material: preparation, characterisation, and its catalytic application, RSC Adv. 8 (2018) 25248–25257.

[25] M. Bhavisha, S. Balamurugan, C.S. Gopinath, A. Sakthivel, The ex situ exsolved Ni–Ru alloy from nickel–ruthenium co-doped SrFeO3−δ perovskite as a potential catalyst for C=C and C=O hydrogenation, Sustain. Energy Fuels 8 (2024) 2839–2849.

[26] A. Sreenavya, S. Ahammed, A. Ramachandran, V. Ganesh, A. Sakthivel, Nickel–ruthenium bimetallic species on hydrotalcite support: a potential hydrogenation catalyst, Catal. Lett. 152 (2022) 848–862.

[27] A. Sreenavya, F. Muhammed, A. Sakthivel, Porous nickel oxide derived from Ni(OH)2: preparation, characterization, and catalytic applications, Emergent Mater. 4 (2021) 803–809.

[28] N.P. Nimisha, S.B. Narendranath, A. Sakthivel, In situ preparation of a nickel-oxy-hydroxide decorated ITQ-2 composite: a hydrodeoxygenation catalyst, Chem. Commun. 60 (2024) 1480–1483.

[29] X. Wang, W. Jiang, R. Yin, P. Sun, Y. Lu, Z. Wu, X. Weng, The role of surface sulfation in mediating the acidity and oxidation ability of nickel modified ceria catalyst for the catalytic elimination of chlorinated organics, J. Colloid Interface Sci. 574 (2020) 251–259.

[30] Y. Wang, X. Wang, J. Gong, X. Fan, Z. Zhou, Improved chlorobenzene oxidation over Fe-Mn oxide by Ni doping: the effect of oxidative ability and surface acidity, Appl. Catal. A: Gen. 644 (2022) 118809.

[31] D. Zhu, M. Liu, S. Li, Y. Mao, J. Chen, Q. Zhang, P. Ning, High efficiency CuOx/TiO2-ZrO2 for chlorobenzenes catalytic oxidation via adjusting surface acidic sites, Appl. Surf. Sci. 639 (2023) 158134.

[32] H. Zhang, X. Gao, B. Gong, S. Shao, C. Tu, J. Pan, Y. Wang, Q. Dai, Y. Guo, X. Wang, Catalytic combustion of CVOCs over MoOx/CeO2 catalysts, Appl. Catal. B: Environ. 310 (2022) 121240.

[33] J. Meng, H. Chen, H. Xie, Q. Zhang, C. Bu, X. Wang, J. Zhang, C. Liu, G. Piao, Plasma-catalytic benzene steam reforming over Ce doped Ni-HAP catalysts: insights into enhanced oxygen activity, Chem. Eng. J. 483 (2024) 149141.

[34] B. Gong, T. Su, X. Xie, H. Ji, Z. Qin, Promotional effects of Mg-substituted Ni/MgxHAP catalysts on carbon resistance during dry reforming of methane, Ind. Eng. Chem. Res 62 (2023) 12935–12948.

[35] Q. Wang, H. Liu, L. Mo, Q. Wei, J. Xu, Effect of pH on mussel shells-originated HAP supported Ag catalysts for catalytic combustion of VOCs, Fuel 360 (2024) 130530.

[36] X. Xu, L. Li, J. Huang, H. Jin, X. Fang, W. Liu, N. Zhang, H. Wang, X. Wang, Engineering Ni3+ cations in NiO lattice at the atomic level by Li+ doping: the roles of Ni3+ and oxygen species for CO oxidation, ACS Catal. 8 (2018) 8033–8045.

[37] J. Pei, B. Peng, H. Lin, W. Chen, Y. Wang, J. Dong, J. Mao, D. Jia, W. Zhu, Z. Zhuang, Single-atom Ru on Al2O3 for highly active and selective 1,2-dichloroethane catalytic degradation, ACS Appl. Mater. Interfaces 13 (2021) 53683–53690.

[38] A. Fihri, C. Len, R.S. Varma, A. Solhy, Hydroxyapatite: A review of syntheses, structure and applications in heterogeneous catalysis, Coord. Chem. Rev. 347 (2017) 48–76.

[39] J. Guo, P.N. Duchesne, L. Wang, R. Song, M. Xia, U. Ulmer, W. Sun, Y. Dong, J.Y.Y. Loh, N.P. Kherani, J. Du, B. Zhu, W. Huang, S. Zhang, G.A. Ozin, High-performance, scalable, and low-cost copper hydroxyapatite for photothermal CO2 reduction, ACS Catal. 10 (2020) 13668–13681.

[40] M. Ibrahim, M. Labaki, J.M. Giraudon, J.F. Lamonier, Hydroxyapatite, a multifunctional material for air, water and soil pollution control: a review, J. Hazard. Mater. 383 (2020) 121139.

[41] L. Silvester, J.-F. Lamonier, R.-N. Vannier, C. Lamonier, M. Capron, A.-S. Mamede, F. Pourpoint, A. Gervasini, F. Dumeignil, Structural, textural and acid–base properties of carbonate-containing hydroxyapatites, J. Mater. Chem. A 2 (2014) 11073–11090.

[42] L. Lv, S. Wang, Y. Ding, L. Zhang, Y. Gao, S. Wang, Mechanistic insights into the contribution of Lewis acidity to brominated VOCs combustion over titanium oxide supported Ru catalyst, Chemosphere 263 (2021) 128112.

[43] X. Chen, J.-J. Li, X. Chen, S.-C. Cai, E.-Q. Yu, J. Chen, H. Jia, MOF-Templated approach for hollow NiOx/Co3O4 catalysts: enhanced light-driven thermocatalytic degradation of toluene, ACS Appl. Nano Mater. 1 (2018) 2971–2981.

[44] S.K. Meher, P. Justin, G. Ranga Rao, Nanoscale morphology dependent pseudocapacitance of NiO: Influence of intercalating anions during synthesis, Nanoscale 3 (2011) 683–692.

[45] G.M. Bai, H.X. Dai, J.G. Deng, Y.X. Liu, K.M. Ji, Porous NiO nanoflowers and nanourchins: highly active catalysts for toluene combustion, Catal. Commun. 27 (2012) 148–153.

[46] S. Wu, H. Zhao, F. Dong, W. Ling, Z. Tang, J. Zhang, Construction of superhydrophobic Ru/TiCeO(x) catalysts for the enhanced water resistance of o-dichlorobenzene catalytic combustion, ACS Appl. Mater. Interfaces 13 (2021) 2610–2621.

[47] W. Liang, Y. Zhu, S. Ren, Q. Li, L. Song, X. Shi, Catalytic combustion of chlorobenzene at low temperature over Ru-Ce/TiO2: high activity and high selectivity, Appl. Catal. A: Gen. 623 (2021) 118257.

[48] L. Silvester, J.-F. Lamonier, J. Faye, M. Capron, R.-N. Vannier, C. Lamonier, J.-L. Dubois, J.-L. Couturier, C. Calais, F. Dumeignil, Reactivity of ethanol over hydroxyapatite-based Ca-enriched catalysts with various carbonate contents, Catal. Sci. Technol. 5 (2015) 2994–3006.

[49] W. Tang, X. Lu, J. Weng, P.-X. Gao, NiO nanosheet array integrated monoliths for low temperature catalytic propane oxidation: a study on the promotion effect of Ce doping, Catal. Today 360 (2021) 194–203.

[50] T. Gao, J. Chen, W. Fang, Q. Cao, W. Su, F. Dumeignil, Ru/MnxCe1Oy catalysts with enhanced oxygen mobility and strong metal-support interaction: exceptional performances in 5-hydroxymethylfurfural base-free aerobic oxidation, J. Catal. 368 (2018) 53–68.

[51] W. Pei, L. Dai, Y. Liu, J. Deng, L. Jing, K. Zhang, Z. Hou, Z. Han, A.

Rastegarpanah, H. Dai, PtRu nanoparticles partially embedded in the 3DOM Ce0.7Zr0.3O2 skeleton: active and stable catalysts for toluene combustion, J. Catal. 385 (2020) 274–288.
[52] P. Zhang, T. Wu, T. Jiang, W. Wang, H. Liu, H. Fan, Z. Zhang, B. Han, Ru–Zn supported on hydroxyapatite as an effective catalyst for partial hydrogenation of benzene, Green. Chem. 15 (2013) 152–159.
[53] X. Dai, X. Wang, Y. Long, S. Pattisson, Y. Lu, D.J. Morgan, S.H. Taylor, J.H. Carter, G.J. Hutchings, Z. Wu, X. Weng, Efficient elimination of chlorinated organics on a phosphoric acid modified CeO2 catalyst: a hydrolytic destruction route, Environ. Sci. Technol. 53 (2019) 12697–12705.
[54] L. Lv, S. Wang, Y. Ding, L. Zhang, Y. Gao, S. Wang, Reaction mechanism dominated by the hard–soft acid–base theory for the oxidation of CH2Cl2 and CH3Br over a titanium oxide-supported Ru catalyst, Ind. Eng. Chem. Res 59 (2020) 7383–7388.
[55] J. Sun, R.A.L. Baylon, C. Liu, D. Mei, K.J. Martin, P. Venkitasubramanian, Y. Wang, Key roles of Lewis acid–base pairs on ZnxZryOz in direct ethanol/acetone to isobutene conversion, J. Am. Chem. Soc. 138 (2016) 507–517.
[56] P. Sun, W. Wang, X. Dai, X. Weng, Z. Wu, Mechanism study on catalytic oxidation of chlorobenzene over MnxCe1-xO2/H-ZSM5 catalysts under dry and humid conditions, Appl. Catal. B: Environ. 198 (2016) 389–397.
[57] X. Weng, P. Sun, Y. Long, Q. Meng, Z. Wu, Catalytic oxidation of chlorobenzene over MnxCe1–xO2/HZSM-5 catalysts: a study with practical implications, Environ. Sci. Technol. 51 (2017) 8057–8066.
[58] Q. Dai, Z. Zhang, J. Yan, J. Wu, G. Johnson, W. Sun, X. Wang, S. Zhang, W. Zhan, Phosphate-functionalized CeO2 nanosheets for efficient catalytic oxidation of dichloromethane, Environ. Sci. Technol. 52 (2018) 13430–13437.
[59] J. Xu, T. White, P. Li, C. He, Y.-F. Han, Hydroxyapatite foam as a catalyst for formaldehyde combustion at room temperature, J. Am. Chem. Soc. 132 (2010) 13172–13173.
[60] F. Bi, X. Zhang, J. Chen, Y. Yang, Y. Wang, Excellent catalytic activity and water resistance of UiO-66-supported highly dispersed Pd nanoparticles for toluene catalytic oxidation, Appl. Catal. B: Environ. 269 (2020) 118767.